

ParticleWNN: a Novel Neural Networks Framework for Solving Partial Differential Equations

Yaohua Zang ^{*} Gang Bao [†]

Abstract

Deep neural networks (DNNs) have been widely used to solve partial differential equations (PDEs) in recent years. In this work, a novel deep learning-based framework named Particle Weak-form based Neural Networks (ParticleWNN) is developed for solving PDEs in the weak form. In this framework, the trial space is defined as the space of DNNs, while the test space consists of functions compactly supported in extremely small regions, centered around particles. To facilitate the training of neural networks, an R-adaptive strategy is designed to adaptively modify the radius of regions during training. The ParticleWNN inherits the benefits of weak/variational formulation, requiring less regularity of the solution and a small number of quadrature points for computing integrals. Additionally, due to the special construction of the test functions, ParticleWNN enables parallel implementation and integral calculations only in extremely small regions. This framework is particularly desirable for solving problems with high-dimensional and complex domains. The efficiency and accuracy of ParticleWNN are demonstrated through several numerical examples, showcasing its superiority over state-of-the-art methods. The source code for the numerical examples presented in this paper is available at <https://github.com/yaohua32/ParticleWNN>.

Keywords. PDEs, Weak Form, Test Function, Small Regions, Deep Neural Networks, Inverse Problems

1 Introduction

In recent decades, deep learning has emerged as a prominent field of study, capturing sustained attention from researchers. Its successful application spans various domains, including natural language processing [1], computer vision [2], and complex tasks like protein structure prediction [3]. Notably, deep neural networks have gained significant traction in the field of numerical PDEs in recent years. In comparison to traditional techniques like the finite element method (FEM), finite difference method (FDM), and finite volume method (FVM), DNN-based methods offer several advantages. These include their mesh-free nature, the capacity to surmount the curse of dimensionality [4, 5, 6], robustness in handling noisy data [7, 8], and intrinsic regularization properties [9, 10]. Consequently, DNN-based approaches are particularly well-suited for tackling a wide array of PDEs and related problems, ranging from high-dimensional PDE problems to PDE-based optimal control and inverse problems. Generally, the PDE-based forward and inverse problems are governed by the following PDE:

$$\mathcal{A}[u(t, \mathbf{x}); \boldsymbol{\gamma}] = 0, \quad \text{in } (0, T] \times \Omega, \quad (1a)$$

$$\mathcal{B}[u(t, \mathbf{x}); \boldsymbol{\gamma}] = g(t, \mathbf{x}), \quad \text{on } [0, T] \times \partial\Omega, \quad (1b)$$

$$\mathcal{I}[u(0, \mathbf{x}); \boldsymbol{\gamma}] = h(\mathbf{x}), \quad \text{on } \Omega, \quad (1c)$$

where Ω is a bounded domain in \mathbb{R}^d with boundary $\partial\Omega$, $T > 0$, and $u(t, \mathbf{x})$ is the solution of the PDE. In this context, \mathcal{A} is the forward operator, representing the type of PDE, which can be parabolic, hyperbolic, or elliptic. The operators \mathcal{B} and \mathcal{I} correspond to the boundary condition and initial condition, respectively.

^{*}School of Engineering and Design, Technische Universität München, München, Germany. Email: yaohua.zang@tum.de.

[†]School of Mathematical Sciences, Zhejiang University, Hangzhou, Zhejiang, China. Email: baog@zju.edu.cn.

The function γ denotes parameters in the PDE; for example, they could represent physical parameters, coefficients, or other relevant quantities. The forward problem involves solving the PDE given the function γ and appropriate boundary conditions (1b) and/or initial conditions (1c). Conversely, the inverse problem aims to determine the function γ from additional boundary or interior measurements of the solution.

Among the existing DNN-based PDE solvers, one popular framework is based on the strong form of PDEs. The most notable one is the physics-informed neural networks (PINN) [11]. PINN approximates the PDE solutions with DNNs and formulates the loss function as a combination of the strong-form PDE residuals and data mismatch. However, the strong-form methods usually require a massive amount of collocation points, leading to a high training cost [12]. Moreover, the non-convex optimization problem obtained by strong-form methods may result in many local minima, making learning complex physical phenomena more challenging [13, 14]. Different from the strong-form methods, the weak-form methods formulate the loss based on the weak/variational form of the PDEs, as demonstrated in various works [15, 16, 17, 18, 19, 6, 7, 20]. This approach offers advantages such as requiring less smoothness in the solution, a reduced number of quadrature points for integral computations, and the ability to facilitate local learning through domain decomposition [20]. Usually, these methods use DNNs to parameterize the trial functions. The difference lies in choosing different types of test functions, including global or piecewise polynomials [20, 18], localized non-overlapping high-order polynomials [19], and DNNs [6, 7]. However, existing weak-form methods define the test functions in the whole domain or sub-domain, which requires accurate integration methods and a large number of integration points to reduce integral approximation errors. Although domain decomposition [17, 19] can alleviate the problem in low-dimensional cases, high-dimensionality makes domain decomposition much more challenging.

In this paper, we introduce ParticleWNN, a novel deep learning-based framework designed for solving PDEs based on the weak form. In this approach, the trial space is defined using DNNs, while the test space is constructed from functions compactly supported in exceedingly small regions, with particles as their centers, serving as local support centers for the test functions. Constructing test functions in this manner offers several advantages. Firstly, the locally defined test functions allow the local training of DNNs and enable parallel implementation. Secondly, since the particles are randomly sampled in the domain and the radius can be extremely small, the proposed method is desirable for high-dimensional and complex domain problems, and avoids the need to calculate integrals over large domains. To enhance the training of the neural network model, we also introduce an R-adaptive strategy, dynamically reducing the upper bound of the compact support radius with each iteration. The efficacy of ParticleWNN is verified through a series of numerical examples. Our primary contributions can be summarized as follows:

- We propose a novel weak-form framework for solving PDEs by using DNNs, where the test space is constructed by functions compactly supported in extremely small regions whose centers are particles.
- We develop several training techniques for the proposed framework to improve its convergence and accuracy.
- We demonstrate the efficiency of the proposed framework through numerical experiments, showcasing its superiority over state-of-the-art methods, particularly in addressing complex problems like PDEs with intricate solutions and inverse problems involving noisy data.

The remainder of the paper is organized as follows. The related works are discussed in Section 2. In Section 3, the ParticleWNN method is proposed for solving PDEs based on the weak formulation with deep neural networks. Section 4 introduces some important implementation details of the ParticleWNN method and techniques to improve algorithm training, and summarizes the algorithm. In Section 5, the accuracy and efficiency of the proposed method are examined through a series of numerical experiments. Finally, conclusions and discussions are drawn in Section 6.

2 Related Works

According to different frameworks, deep learning-based PDE methods can be roughly divided into four categories: the strong-form methods, the weak-form methods, the hybrid methods of traditional methods and deep learning, and methods based on neural operators. Typically, the strong-form methods utilize

DNNs to approximate the solution of the equation. Collocation points are generated on the domain and the domain boundary to evaluate the strong-form residuals of the governing equations in the domain and the mismatches of solutions on the boundary, respectively. Then, the network parameters are learned by minimizing the weighted combination of residuals and mismatches. Representative methods of this type include the deep Galerkin method (DGM) [5] and the physical-informed neural networks (PINN) method [11]. Building upon the PINN framework, many methods have been proposed to address specific PDEs or enhance PINN’s capabilities. These include methods for solving fractional advection-diffusion equations (fPINN) [21], handling Navier-Stokes equations (NSFnets) [22], addressing PDE-based inverse problems (B-PINN) [23], and dealing with PDEs in irregular domain (PhyGeoNet) [24]; Various improvements to PINN have also been suggested, such as adaptive collocation points strategies [25, 26], domain decomposition techniques [13, 12], loss modification approaches [27, 28], and new training strategies [14]. For additional information on strong-form methods, refer to [29], which provides a comprehensive exploration of these techniques

The weak-form methods, on the other hand, formulate the loss based on the weak or variational form of the PDEs. Based on the variational principle, the Deep Ritz method (DeepRitz) [15] solves PDEs by minimizing an energy function, which was further extended to PDEs with essential boundary conditions in the deep Nitsche method [16]. In [17], a deep domain decomposition method (D3M) was proposed based on the variational principle. In [6, 7], the weak adversarial network (WAN) was proposed based on the weak form to convert the problem into an operator norm minimization problem. The variational neural networks (VarNet) method [18] is based on the Petrov-Galerkin method. In this method, the trial function is approximated by DNN, and the test functions are a set of piecewise polynomials that have compact support in the domain. The variational formulation of PINN (VPINN) [20] has a similar formulation, except that the test functions are chosen to be polynomials with globally compact support over the domain. Combined with domain decomposition, the hp-VPINN [19] was developed based on the sub-domain Petrov-Galerkin method. It divides the domain into multiple non-overlapping subdomains (h-refinement) and sets test functions as localized non-overlapping high-order polynomials (p-refinement).

The hybrid methods combine traditional methods with DNN-based methods to overcome the shortcomings of pure DNN-based methods. In [30], the classical Galerkin method was combined with neural networks to solve initial boundary value problems. In [31], a DiscretizationNet method was developed to combine the finite volume discretization with a generative CNN-based encoder-decoder for solving the Navier-Stokes equations. The coupled automatic-numerical differentiation PINN (CAN-PINN) was developed in [32], where the numerical differentiation-inspired method was coupled with the automatic differentiation to define the loss function. Furthermore, DNN-based methods were integrated with the finite difference method in [33, 34] and the finite element method in [35].

Recent advancements in solving PDEs have seen the emergence of operator learning methods [36, 37, 38, 39, 40], which focus on learning mappings between function spaces. These methods differ from other approaches discussed earlier, as they rely on high-precision numerical PDE methods, typically classical methods like the FEM and FVM, to generate the training data. The advantage of these methods lies in providing rapid numerical solution predictions for a specific class of PDEs. In [37], the DeepONet method was proposed to learn continuous nonlinear operators. It is composed of two sub-networks: a branch net for the input fields and a trunk net for the locations of the output field. Based on the DeepONet, the DeepM&Mnet framework was developed for simulating multiphysics and multiscale problems in [40]. In [36], the authors introduced the concept of the neural operator and instantiated it through graph kernel networks designed to approximate mappings between infinite-dimensional spaces. Inspired by the classical multipole methods, this method was then generalized to the multi-level case in [39] to capture interaction at all ranges. In [38], the Fourier Neural Operators (FNOs) method was proposed using convolution-based integral kernels within neural operators, where kernels can be efficiently evaluated in the Fourier space.

3 Methodology

3.1 The ParticleWNN framework

To illustrate the proposed method, we consider the classical Poisson equation with the Dirichlet boundary condition:

$$\begin{cases} -\Delta u(\mathbf{x}) = f(\mathbf{x}), & \text{in } \Omega \subset \mathbb{R}^d, \\ u(\mathbf{x}) = g(\mathbf{x}), & \text{on } \partial\Omega. \end{cases} \quad (2)$$

The weak formulation of Poisson’s equation (2) involves finding a function in $\{u \in H^1(\Omega) | u|_{\partial\Omega} = g\}$ such that, for all test functions $\varphi \in H_0^1(\Omega)$, the following equation holds:

$$\int_{\Omega} \nabla u \cdot \nabla \varphi \, d\mathbf{x} = \int_{\Omega} f \varphi \, d\mathbf{x}, \quad (3)$$

where $H^1(\Omega)$ denotes the Sobolev space of functions with square-integrable derivatives and $H_0^1(\Omega)$ contains $H^1(\Omega)$ functions with zero boundary conditions. Under appropriate conditions for f and g , the weak form (3) allows a unique solution u , referred to as the *weak solution* [41]. Generally, weak-form DNN-based methods approximate the function u with a neural network $u_{NN}(\mathbf{x}; \theta)$, which usually consists of l hidden layers with \mathcal{N}_i neurons in each layer and activation function $\sigma(\cdot)$ that takes the following form:

$$u_{NN}(\mathbf{x}; \theta) = T^{(l+1)} \circ T^l \circ T^{(l-1)} \circ \dots \circ T^{(1)}(\mathbf{x}). \quad (4)$$

Here, the linear mapping $T^{(l+1)} : \mathbb{R}^{\mathcal{N}_i} \rightarrow \mathbb{R}$ indicates the output layer, and $T^{(i)}(\cdot) = \sigma(\mathbf{W}_i \cdot + \mathbf{b}_i)$, $i = 1, \dots, l$ are nonlinear mappings with weights $\mathbf{W}_i \in \mathbb{R}^{\mathcal{N}_i \times \mathcal{N}_{i-1}}$ and biases $\mathbf{b}_i \in \mathbb{R}^{\mathcal{N}_i}$. The network parameters are collected in $\theta = \{\mathbf{W}_i, \mathbf{b}_i\}_{i=1}^{l+1}$. Usually, the network is trained by minimizing a loss function, typically defined as the root mean square (RMS) or mean squared error (MSE) of the weak-form residuals, along with some penalty terms. Following [20, 19], we denote \mathcal{R} as the weak-form residual in (3):

$$\mathcal{R}(u_{NN}; \varphi) = \int_{\Omega} \nabla u_{NN} \cdot \nabla \varphi \, d\mathbf{x} - \int_{\Omega} f \varphi \, d\mathbf{x}. \quad (5)$$

Different choices of the test functions vary in different weak-form methods. For instance, the VarNet [18] defines the test functions as a set of piecewise polynomials with compact support over the entire domain, the VPINN [20] selects test functions as polynomials with globally compact support, the hp-VPINN [19] employs localized non-overlapping high-order polynomials, and the WAN [6] represents the test space with DNNs. The special feature of our work is choosing test functions to be compactly supported functions defined in small neighborhoods $B(\mathbf{x}^c, R) \subset \Omega$, where \mathbf{x}^c is a particle in Ω and R is the radius of the neighborhood. This choice offers advantages such as enabling the DNN to focus on extremely local regions, avoiding integration over the entire domain, and facilitating parallelization. Specifically, we choose the compactly supported radial basis functions (CSRBFs) as test functions in this work. Usually, the CSRBFs defined in $B(\mathbf{x}^c, R)$ have the following form:

$$\varphi(r) = \begin{cases} \varphi_+(r), & r(\mathbf{x}) \leq 1, \\ 0, & r(\mathbf{x}) > 1, \end{cases} \quad (6)$$

where $r(\mathbf{x}) = \|\mathbf{x} - \mathbf{x}^c\|_2 / R$. In fact, any functions in $H^1(\Omega)$ that are compactly supported in $B(\mathbf{x}^c, R)$ can be used as test functions. To improve training efficiency, we use multiple test functions to formulate the loss function. We generate N_p particles $\{\mathbf{x}_i^c\}_i^{N_p}$ and the corresponding $\{R_i\}_i^{N_p}$ randomly or with predefined rules in the domain¹, and then define N_p CSRBFs $\{\varphi_i\}_i^{N_p}$ in each small neighbourhood $B(\mathbf{x}_i^c, R_i)$. Therefore, we obtain the MSE of the weak-form residuals:

$$\mathcal{L}_{\mathcal{R}} = \frac{1}{N_p} \sum_{i=1}^{N_p} |\mathcal{R}(u_{NN}; \varphi_i)|^2. \quad (7)$$

¹To ensure that $B(\mathbf{x}^c, R) \subset \Omega$, we generate R first, and then sample \mathbf{x}^c in $\tilde{\Omega} = \{\mathbf{x} \in \Omega | \text{dist}(\mathbf{x}, \partial\Omega) \geq R\}$.

For the boundary condition (and/or initial condition), we can treat it as a penalty term:

$$\mathcal{L}_{\mathcal{B}} = \frac{1}{N_{bd}} \sum_{j=1}^{N_{bd}} |\mathcal{B}[u_{NN}(\mathbf{x}_j)] - g(\mathbf{x}_j)|^2, \quad (8)$$

where $\{\mathbf{x}_j\}_{j=1}^{N_{bd}}$ are sampled points on the $\partial\Omega$. Finally, we formulate our loss function as:

$$\mathcal{L}(\theta) = \lambda_{\mathcal{R}} \mathcal{L}_{\mathcal{R}} + \lambda_{\mathcal{B}} \mathcal{L}_{\mathcal{B}}, \quad (9)$$

where $\lambda_{\mathcal{R}}$ and $\lambda_{\mathcal{B}}$ are weight coefficients in the loss function.

3.2 Calculation of the loss

To evaluate the loss in (9), we need to calculate N_p integrals that are defined in $B(\mathbf{x}_i^c, R_i)$, $i = 1, \dots, N_p$. A straightforward way to evaluate integrals is to use the Monte Carlo integration. Unfortunately, it requires an immense sample size to ensure admissible integration errors. An alternative is the quadrature rule method. This method works efficiently in low-dimensional case or when the integrand is simple. However, in the case of high dimensional problems and complicated integrands, one needs to further increase the quadrature points, thus greatly increasing the computational cost. Other numerical techniques, such as sparse grids [42] and quasi-Monte Carlo integration [43], can also be employed. In our framework, thanks to the special construction of the test functions, we only need to evaluate integrals in the small region $B(\mathbf{x}_i^c, R_i)$ rather than the entire domain. As u_{NN} is typically nearly constant within a small region, the integrand simplifies. Consequently, we can achieve similar accuracy with significantly fewer integration points compared to integrating over the entire domain or sub-domain. By applying a simple coordinate transformation, we convert the calculation of integrals over N_p small regions into computations over a standard region $B(\mathbf{0}, 1)$. The coordinate transformation $\mathbf{x} = \mathbf{s}R_i + \mathbf{x}_i^c$ can be applied in (5), resulting in:

$$\begin{aligned} \mathcal{R}(u_{NN}; \varphi_i) &= \int_{B(\mathbf{x}_i^c, R_i)} \nabla_{\mathbf{x}} u_{NN} \cdot \nabla_r \varphi_i \cdot \nabla_{\mathbf{x}} r \, d\mathbf{x} - \int_{B(\mathbf{x}_i^c, R_i)} f \varphi_i \, d\mathbf{x}, \\ &= R_i^d \left(\int_{B(\mathbf{0}, 1)} \nabla_{\mathbf{x}} u_{NN}(\mathbf{x}) \cdot \nabla_r \varphi_i \cdot \nabla_{\mathbf{x}} r \, d\mathbf{s} - \int_{B(\mathbf{0}, 1)} f(\mathbf{x}) \varphi_i \, d\mathbf{s} \right), \end{aligned} \quad (10)$$

where we use $\nabla_{\mathbf{x}} \varphi_i = \nabla_r \varphi_i \cdot \nabla_{\mathbf{x}} r$. This allows us to generate one set of integration points in $B(\mathbf{0}, 1)$ to calculate N_p integrals. For example, assume that $\{\mathbf{s}_k\}_{k=1}^m$ are K_{int} integration points generated from $B(\mathbf{0}, 1)$ and $\{w_k\}_{k=1}^m$ are the corresponding weights. Then, we denote $\mathbf{x}_k^{(i)} := \mathbf{s}_k * R_i + \mathbf{x}_i^c$ and approximate $\mathcal{R}(u_{NN}; \varphi_i)$ by:

$$\mathcal{R}(u_{NN}; \varphi_i) \approx \frac{R_i^d \mathcal{V}_{B(\mathbf{0}, 1)}}{K_{int}} \sum_{k=1}^{K_{int}} w_k \left(\nabla_{\mathbf{x}} u_{NN}(\mathbf{x}_k^{(i)}) \cdot \nabla_r \varphi_i(\mathbf{x}_k^{(i)}) \cdot \nabla_{\mathbf{x}} r(\mathbf{x}_k^{(i)}) - f(\mathbf{x}_k^{(i)}) \varphi_i(\mathbf{x}_k^{(i)}) \right), \quad (11)$$

where $\mathcal{V}_{B(\mathbf{0}, 1)}$ indicates the volume of $B(\mathbf{0}, 1)$. Consequently, the loss (7) can be approximated by:

$$\mathcal{L}_{\mathcal{R}} \approx \frac{\mathcal{V}_{B(\mathbf{0}, 1)}^2}{N_p K_{int}^2} \sum_{i=1}^{N_p} R_i^{2d} \left(\sum_{k=1}^{K_{int}} w_k \left(\nabla_{\mathbf{x}} u_{NN}(\mathbf{x}_k^{(i)}) \cdot \nabla_r \varphi_i(\mathbf{x}_k^{(i)}) \cdot \nabla_{\mathbf{x}} r(\mathbf{x}_k^{(i)}) - f(\mathbf{x}_k^{(i)}) \varphi_i(\mathbf{x}_k^{(i)}) \right) \right)^2. \quad (12)$$

From (12), we can see that the value of $\mathcal{L}_{\mathcal{R}}$ depends on R_i^{2d} . To avoid the training failure, we remove R_i^{2d} in (12). We also remove the fixed term $\mathcal{V}_{B(\mathbf{0}, 1)}^2$, which does not affect the training of the model. We denote $\tilde{\mathcal{L}}_{\mathcal{R}}$ as the approximation of $\mathcal{L}_{\mathcal{R}}$ with R_i^{2d} and $\mathcal{V}_{B(\mathbf{0}, 1)}^2$ removed. Then, the loss function (9) is modified and approximated as:

$$\begin{aligned} \tilde{\mathcal{L}}(\theta) &= \frac{\lambda_{\mathcal{R}}}{N_p K_{int}^2} \sum_{i=1}^{N_p} \left(\sum_{k=1}^{K_{int}} w_k \left(\nabla_{\mathbf{x}} u_{NN}(\mathbf{x}_k^{(i)}) \cdot \nabla_r \varphi_i(\mathbf{x}_k^{(i)}) \cdot \nabla_{\mathbf{x}} r(\mathbf{x}_k^{(i)}) - f(\mathbf{x}_k^{(i)}) \varphi_i(\mathbf{x}_k^{(i)}) \right) \right)^2 \\ &\quad + \frac{\lambda_{\mathcal{B}}}{N_{bd}} \sum_{j=1}^{N_{bd}} \left(\mathcal{B}[u_{NN}(\mathbf{x}_j)] - g(\mathbf{x}_j) \right)^2. \end{aligned} \quad (13)$$

4 The Implementation Details

In this section, we discuss some implementation details and training techniques that will improve the performance of the proposed ParticleWNN.

Selection of test functions. In our framework, while the construction of the compact support of the test functions is determined, the types of test functions themselves can be very diverse. In fact, any functions in the H_0^1 space can be considered test functions providing an infinite number of possible choices. For different integration methods, the selection of test functions have varying effects on the integration error, ultimately influencing the accuracy of the method. In the numerical examples presented in this paper, we opt for meshgrid integration points and choose Compactly Supported Radial Basis Functions (CSRBFs) as test functions. There are various types of CSRBFs to choose from, such as the Bump function [44], Wendland’s function [45], Wu’s function [46], Buhmann’s function [47], among others. Typically, we consider the following Wendland’s type CSRBFs:

$$\phi_{d,2}(r) = \begin{cases} \frac{(1-r)^{l+2}}{3} [(l^2 + 4l + 3)r^2 + (3l + 6)r + 3], & r < 1, \\ 0, & r \geq 1, \end{cases} \quad (14)$$

where $l = \lfloor d/2 \rfloor + 3$, d is the dimension of the domain, and $\lfloor \cdot \rfloor$ indicates the flooring function.

R-adaptive strategy. In the ParticleWNN framework, the parameter R plays a crucial role in determining the size of the interest area of the network model u_{NN} . If R is too large, there will be increased overlaps between compact supports, leading to the loss becoming insensitive to changes in particles. Additionally, a large R often implies a more complex integrand, resulting in a larger approximation error for the integral. However, R should not be too small, as it may cause precision loss in floating-point numbers. In this work, we dynamically generate R_i for each particle \mathbf{x}_i^c from a range $[R_{min}, R_{max}]$ where R_{min} is a small fixed number and $R_{max} (\geq R_{min})$ is another small number that varies with iterations. Generally, there are three common ways for R_{max} to change with iterations:

- **R-ascending:** R_{max} gradually increases with iterations until it reaches a specified upper bound.
- **R-fixed:** R_{max} remains unchanged.
- **R-descending:** R_{max} gradually decreases with iterations until a given lower bound is reached.

In the experiment, we observed that the **R-descending** strategy yielded the best performance (refer to details in the appendix A). Therefore, we adopt the **R-descending** strategy for training the ParticleWNN.

Adaptive selection of particles. A common way to improve the training of ParticleWNN is to select the particles with some smart rules. In this paper, we found that the *topK* technique can improve the performance of the proposed ParticleWNN (see the appendix B for details). The implementation of the *topK* technique is as follows: initially, we randomly sample N_p particles in the domain. Subsequently, we evaluate the square residuals for each particle with (11). Finally, we choose the *topK* ($\leq N_p$) particles with the largest residuals to calculate the loss.

Summary of the algorithm. We summarize the ParticleWNN algorithm in Algorithm 1. It is worth noting that, although the implementation of parallelization is not included in Algorithm 1, achieving parallelization is straightforward. The steps involve distributing the computation of N_p weak residuals and their gradients to $M \leq N_p$ machines for simultaneous processing, thus achieving parallelization.

5 Experiments

In this section, we present a series of numerical experiments to demonstrate the ParticleWNN method’s effectiveness in overcoming the common challenge of requiring a large number of integration points in weak-form

Algorithm 1 The ParticleWNN Algorithm

- 1: **Input:** $N_p, N_{bd}, K_{int}, R_{min}, R_{max}, \lambda_{\mathcal{R}}, \lambda_{\mathcal{B}}, topK$, learning rate τ_{θ} , and maximum iterations $maxIter$.
 - 2: **Initialize:** Network architecture $u_{NN}(\mathbf{x}; \theta) : \Omega \rightarrow \mathbb{R}$, where θ indicates network parameters.
 - 3: **while** iterations $< maxIter$ **do**
 - 4: Generate radius $\{R_i\}_{i=1}^{N_p} \sim \text{Unif}[R_{min}, R_{max}]$, particles $\{\mathbf{x}_i^c \in \tilde{\Omega} : i \in [N_p]\}$, data points $\{\mathbf{x}_j \in \partial\Omega : j \in [N_{bd}]\}$, and integral points $\{\mathbf{s}_k \in B(\mathbf{0}, 1) : k \in [K_{int}]\}$.
 - 5: Get integral points for each region $B(\mathbf{x}_i^c, R_i)$: $\mathbf{x}_k^{(i)} = \mathbf{s}_k R_i + \mathbf{x}_i^c, k \in [K_{int}], i \in [N_p]$.
 - 6: Calculate residuals $\mathcal{R}(u_{NN}; \varphi_i)$ with (11) and evaluate the loss $\tilde{\mathcal{L}}(\theta)$ with $topK$ residuals.
 - 7: Update network parameters with SGD: $\theta \leftarrow \theta - \tau_{\theta} \nabla_{\theta} \tilde{\mathcal{L}}(\theta)$.
 - 8: **end while**
 - 9: **Output:** The trained network $u_{NN}(\mathbf{x}; \theta)$.
-

methods. We compare our proposed method with two widely recognized weak-form DNN-based approaches: the DeepRitz method and the VPINN method. Furthermore, we include a comparison with the strong-form method, PINN, to highlight ParticleWNN’s relative advantages in solving problems with intricate solutions. Since our paper primarily emphasizes methodological differences in solving PDEs and related problems, we limit our comparisons to the classic PINN method without special training techniques². In the following, we refer to the PINN method without special training techniques as the vanilla PINN method.

Experimental setups. Without specific clarifications, we choose the trial function u_{NN} as a ResNet with 4 hidden layers and 50 nodes in each layer, and provide the activations in specific problems. During the training process, we randomly sample N_p particles in the domain and $N_{bd} = 2d\tilde{N}_{bd}$ points (\tilde{N}_{bd} for each of $2d$ sides) on the boundary. we sample the radius R_i from $[R_{min}, R_{max}]$ for each region, where R_{max} decreases linearly with the number of iterations. We set $R_{min} = 10^{-6}$, $R_{max} = 10^{-4}$, $\lambda_{\mathcal{R}} = 1$, $\lambda_{\mathcal{B}} = 5$, $maxIter = 20000$, and generate K_{int} integration points in $B(\mathbf{0}, 1)$ to evaluate integrals. We adopt the Adam optimizer with $\tau_{\theta} = 0.001$ and apply the StepLR scheduler with a step size of 1 epoch and a $\gamma = 1 - 2./maxIter$. We use the Relative error $\|u_{NN} - u\|_2 / \|u\|_2$ and the maximum absolute error (MAE) $\max |u_{NN} - u|$ as evaluation metrics and run each example with 5 random seeds to obtain the mean and the standard deviation. For the 1D poisson problem (15), all related experiments were executed using the Google Colab [48] with a Tesla T4 GPU. For other problems, all experiments were executed using the Kaggle Notebook [49] with a Tesla P100 GPU.

5.1 The 1D Poisson’s Equation

We first consider the following one-dimensional Poisson’s equation:

$$\begin{cases} -\frac{\partial^2 u}{\partial x^2}(x) = f(x), & x \in \Omega = (-1, 1), \\ u(x) = g(x), & x \in \partial\Omega. \end{cases} \quad (15)$$

We construct a solution $u(x) = x \cos(\omega x)$ for (15) and use it to calculate the forcing term $f(x)$ and boundary condition $g(x)$. Previous work [50] has shown that the vanilla PINN struggles to solve this problem with a Fully Connected Feedforward Neural Network using Tanh activation. Here, we opt for a composite function of Tanh and Sine as the activation in the network models. We set $N_p = 200$, $topK = 150$, $K_{int} = 50$, and $\tilde{N}_{bd} = 1$ for the proposed method. For comparison, we generate 10000 integration points in Ω for the DeepRitz method and 10000 ($topK = 7500$) collocation points for the vanilla PINN. We set the number of integration points to $N_{int} = 200$ and the number of test functions to $N_{test} = 50$ for the VPINN method. Other parameters maintain consistent settings.

We explore two different frequency scenarios: a low-frequency case with $\omega = 2\pi$ and a high-frequency case with $\omega = 15\pi$. The results for these cases are summarized in Table 1, and visualized in Figures 1 and 2 for the low and high-frequency cases, respectively. In the low-frequency scenario, as illustrated in Figure 1, both the DeepRitz and VPINN methods show faster convergence than ParticleWNN. However, their accuracy falls

²It’s worth noting that most of these techniques are also applicable to the ParticleWNN method.

significantly short of ParticleWNN due to the limitation imposed by integration points. Although vanilla PINN achieves higher accuracy than ParticleWNN, it does so at the cost of slower convergence and increased computation time, as evident from Table 1. In contrast, as seen in Figure 2 for the high-frequency case, ParticleWNN outperforms vanilla PINN, primarily because the error introduced by integral approximation in ParticleWNN becomes negligible compared to the approximation error of the neural network model in high-frequency scenarios. This underscores ParticleWNN’s advantage in solving problems with complex solutions. Furthermore, the limitation of integration points becomes more pronounced for the DeepRitz and VPINN methods in the high-frequency case. The VPINN method, in particular, struggles to produce acceptable solutions. Figure 2(c) shows that the relative error of the VPINN method initially decreases and then increases during the training process, indicative of overfitting due to insufficient integration points. To validate the impact of increased integration points on the VPINN method, we doubled the integration points while keeping other settings constant. With this adjustment, the VPINN method achieved an average relative error of 0.1004 ± 0.0178 , an average MAE of 0.1296 ± 0.0266 , and an average computation time of 588.70 ± 5.00 . The results demonstrate an obvious improvement, but it still falls short of the performance achieved by the ParticleWNN method.

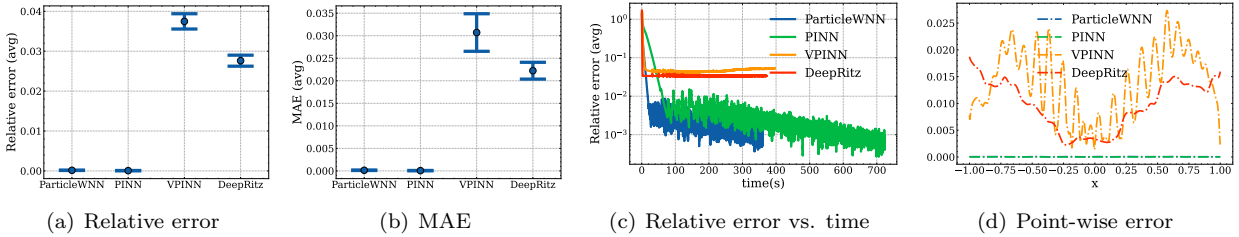


Figure 1: The performance of different methods in solving problem (15) with frequency $\omega = 2\pi$. (a) Average Relative errors; (b) Average MAEs; (c) Average Relative errors vs. Average computation times; (d) Average point-wise errors.

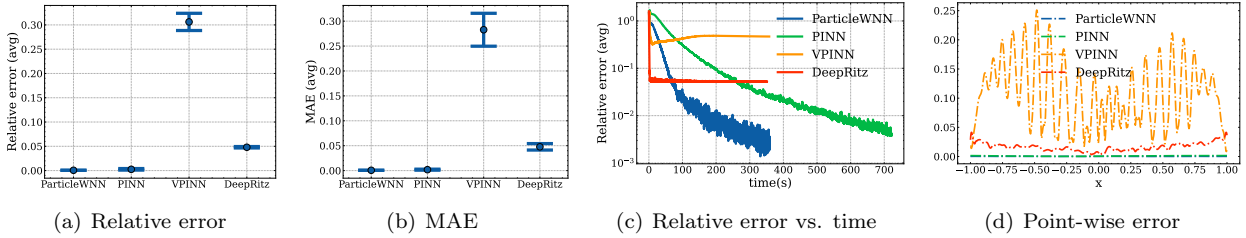


Figure 2: The performance of different methods in solving the Poisson problem (15) with frequency $\omega = 15\pi$. (a) Average Relative errors; (b) Average MAEs; (c) Average Relative errors vs. Average computation times. (d) Average point-wise errors.

Table 1: Experiment results for the Poisson problem (15).

		ParticleWNN	vanilla PINN	VPINN	DeepRitz
$\omega = 2\pi$	Relative error	$1.46e^{-4} \pm 3.86e^{-5}$	$6.71e^{-5} \pm 3.54e^{-5}$	$3.75e^{-2} \pm 1.91e^{-3}$	$2.76e^{-2} \pm 1.38e^{-3}$
	MAE	$1.39e^{-4} \pm 5.05e^{-5}$	$6.31e^{-5} \pm 3.43e^{-5}$	$3.07e^{-2} \pm 4.17e^{-3}$	$2.22e^{-2} \pm 1.86e^{-3}$
	Time(s)	360.05 ± 1.92	723.51 ± 2.89	396.39 ± 9.13	371.18 ± 3.99
$\omega = 15\pi$	Relative error	$5.86e^{-4} \pm 8.28e^{-5}$	$2.57e^{-3} \pm 1.59e^{-3}$	$3.06e^{-1} \pm 1.77e^{-2}$	$4.80e^{-2} \pm 1.44e^{-3}$
	MAE	$6.04e^{-4} \pm 7.43e^{-5}$	$1.85e^{-3} \pm 1.01e^{-3}$	$2.83e^{-1} \pm 3.30e^{-2}$	$4.77e^{-2} \pm 6.48e^{-3}$
	Time(s)	359.63 ± 1.86	722.16 ± 11.67	357.92 ± 1.78	350.57 ± 0.95

5.2 The Allen-Cahn equation

We then consider the following nonlinear Allen-Cahn equation

$$\begin{cases} u_t - \lambda u_{xx} + 5u^3 - 5u = 0, & t \in (0, 1], x \in [-1, 1], \\ u(x, 0) = x^2 \cos(\pi x), \\ u(t, -1) = u(t, 1), u_x(t, -1) = u_x(t, 1), \end{cases} \quad (16)$$

where $\lambda = 0.0001$. The equation is difficult to solve due to its sharp solution (see Figure 3(a)). To solve this problem with the ParticleWNN, we select the test function $\varphi(\mathbf{x})$ in Algorithm 1 such that it depends only on \mathbf{x} and multiply it with both sides of Equation (16). Then, we get the weak formulation through variation:

$$\int_{\Omega} (u_t + 5u^3 - 5u)\varphi \, d\mathbf{x} + \lambda \int_{\Omega} \nabla_{\mathbf{x}} u \cdot \nabla_{\mathbf{x}} \varphi \, d\mathbf{x} = 0, \quad t \in (0, 1]. \quad (17)$$

We handle the initial value conditions similarly to the boundary conditions. We sample $N_{init} = 200$ points in Ω to evaluate the mismatch of initial conditions and set the corresponding loss weight as $\lambda_{\mathcal{T}} = 50$. To evaluate the weak-form residuals, we sample $N_t = 100$ time points in $(0, 1]$. At each time point, we randomly sample $N_p = 50$ particles in Ω and set $K_{int} = 25$ to calculate the integrals in (17). For other parameters, we set $N_{bd} = 200$, $topK = 4000$, $\lambda_{\mathcal{R}} = 100$, $maxIter = 50000$, and increase the number of neurons per layer in the ResNet to 100 and use the composite function of Tanh and Sine as the activation. For comparison, we generate 125,000 ($topK = 100,000$) collocation points for the vanilla PINN to evaluate the strong residuals and keep other settings consistent with ParticleWNN. For the VPINN method, we employ $N_t = 100$ time points, along with $N_{test} = 50$ test functions and $N_{int} = 25$ integration points.

The experimental results are summarized in Table 2 and depicted in Figure 3. Figure 3(c) indicates that ParticleWNN achieves higher accuracy and faster convergence than both the vanilla PINN and the VPINN method. The Table 2 also shows that the ParticleWNN takes almost half the computation time of the vanilla PINN.

Table 2: Experiment results for the Allen-Cahn problem (16).

	ParticleWNN	vanilla PINN	VPINN
Relative error	0.073 \pm 0.015	0.323 \pm 0.167	0.236 \pm 0.079
MAE	0.529 \pm 0.058	1.243 \pm 0.402	1.158 \pm 0.368
Time(s)	6622.33 \pm 29.47	12332.18 \pm 70.20	4942.12 \pm 13.36

5.3 The 2D incompressible Navier-Stokes equation

We proceed to solve a steady 2D incompressible NS equation, using the Kovaszny flow as an example. In non-dimensional form, the mathematical model is given by:

$$\begin{cases} -\nu \Delta \mathbf{u} + (\mathbf{u} \cdot \nabla) \mathbf{u} + \nabla p = 0, & \text{in } \Omega = [-1, 1] \times [-1, 1], \\ \nabla \cdot \mathbf{u} = 0, & \text{in } \Omega \end{cases} \quad (18)$$

where ν is the viscosity coefficient, and $\mathbf{u} = (u, v)$ and p are the velocity field and the pressure field, respectively. The analytical solution for this equation is given by [51]:

$$u(x, y) = 1 - e^{\lambda x} \cos(\omega y), \quad v(x, y) = \frac{\lambda}{\omega} e^{\lambda x} \sin(\omega y), \quad p(x, y) = \frac{1}{2}(1 - e^{2\lambda x}), \quad (19)$$

where

$$\lambda = \frac{1}{2\nu} - \sqrt{\frac{1}{4\nu^2} + \omega^2}.$$

In our setup, we choose $\nu = 0.025$ and $\omega = 3\pi$. To solve the problem, we approximate the pressure p with one network and use another network with two outputs to approximate both u and v . We adopt the Tanh

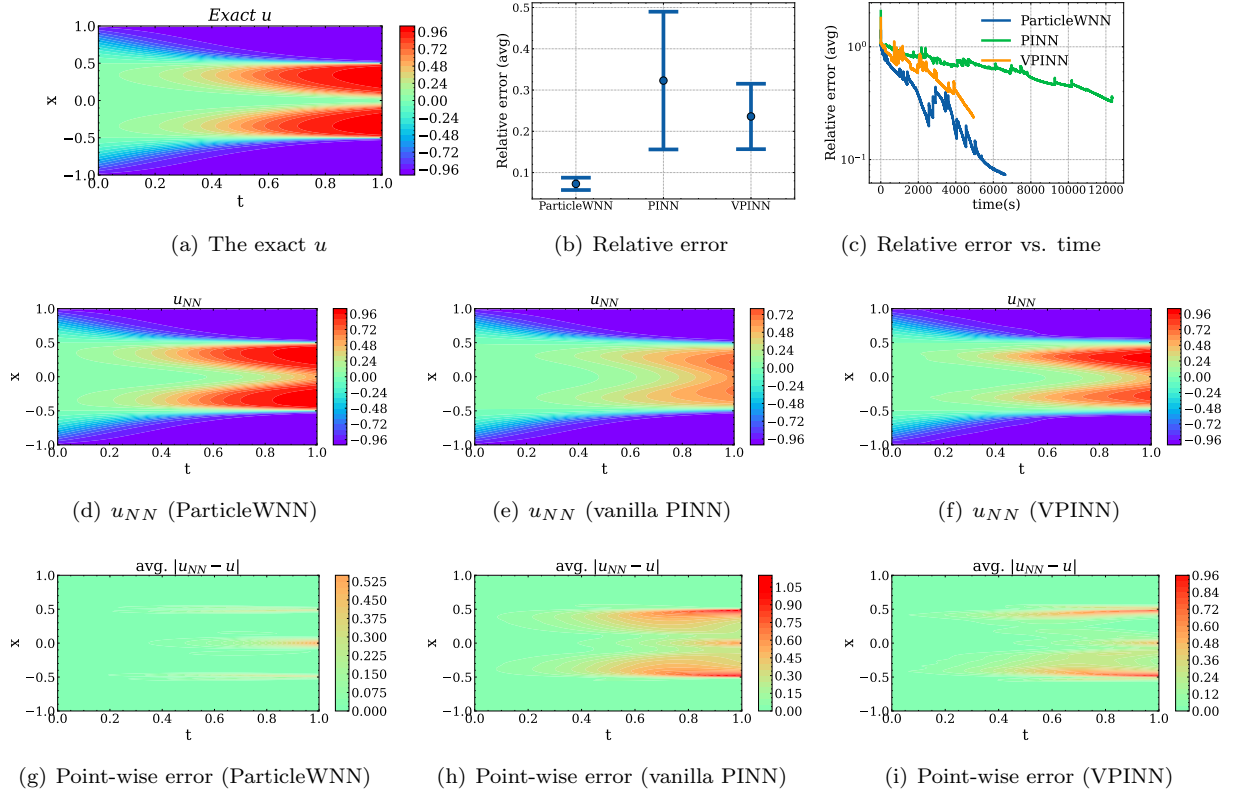


Figure 3: The performance of different methods in solving the Allen-Cahn problem (16). (a) The exact u ; (b) Average Relative errors; (c) Average Relative errors vs. Average computation times. (d), (e), (f) The average u_{NN} obtained by different methods; (g), (h), (i) The average point-wise errors obtained by different methods.

Table 3: Experiment results for the steady NS problem (18).

	ParticleWNN	vanilla PINN	VPINN
Relative error for u	$1.34e^{-3} \pm 7.41e^{-5}$	$3.58e^{-3} \pm 6.78e^{-4}$	$8.99e^{-1} \pm 1.69e^{-3}$
MAE for u	$1.44e^{-2} \pm 2.04e^{-3}$	$3.50e^{-2} \pm 5.00e^{-3}$	9.02 ± 0.33
Relative error for v	$3.41e^{-3} \pm 1.94e^{-4}$	$9.67e^{-3} \pm 1.16e^{-3}$	0.95 ± 0.03
MAE for v	$7.01e^{-3} \pm 1.25e^{-3}$	$3.09e^{-2} \pm 5.74e^{-3}$	1.99 ± 0.06
Relative error for p	$4.52e^{-4} \pm 3.60e^{-5}$	$2.68e^{-3} \pm 4.86e^{-4}$	$7.38e^{-1} \pm 1.10e^{-2}$
MAE for p	$3.25e^{-2} \pm 9.22e^{-3}$	$2.73e^{-1} \pm 5.94e^{-2}$	29.61 ± 2.46
Time (s)	3182.74 ± 2.80	7703.80 ± 29.23	2983.63 ± 3.27

activation function for the DNN models. In the ParticleWNN method, we set $N_p = 250$ (without $topK$), $K_{int} = 124$, $\tilde{N}_{bd} = 250$. For a fair comparison, the vanilla PINN method utilizes 31,000 collocation points, while the VPINN method use $N_{test} = 50$ test functions and $N_{int} = 625$ integration points. Other settings are consistent across all methods.

After $maxIter = 100,000$ iterations, the results are summarized in Table 3. Figure 4 displays the numerical predictions of u , v , and p obtained by each method, along with corresponding relative error plots over time. From Figure 4, it is evident that the VPINN method struggles to achieve an accurate solution due to the limitations imposed by insufficient integration points. In contrast, both the vanilla PINN and ParticleWNN methods deliver accurate solutions. The ParticleWNN method also demonstrates faster convergence than the vanilla PINN, with the added benefit of consuming less than half the computation time (details in Table 3). This advantage arises from ParticleWNN’s avoidance of higher-order derivative computations for u , v , and p .

5.4 Inverse Problems

The particleWNN can also be applied to solve inverse problems. Typically, we consider the following coefficient identification problem often used to verify the effectiveness of DNN-based methods:

$$-\nabla \cdot (a(x, y)\nabla u) = f(x, y), \quad (x, y) \in \Omega = [-1, 1] \times [-1, 1], \quad (20)$$

where u is the solution of the equation, f indicates the source term, and $a \in \{a \in L^\infty(\Omega) : 0 < \underline{a} \leq a(x, y) \leq \bar{a} \text{ a.e. in } \Omega\}$ represents the coefficient. In the inverse problem, given the source term f , the objective is to identify the coefficient a with inexact measurements u^δ where δ indicates Gaussian noise. We set the exact coefficient as

$$a(x, y) = 0.1 + \exp^{-\frac{(x-x_1)^2}{\sigma_1} + \frac{(y-y_1)^2}{\sigma_2}}, \quad (21)$$

where σ_1, σ_2 are sampled from $[0.01, 0.5]$, and x_1, y_1 are sampled from $[-0.5, 0.5]$, as shown in Figure 5(a). For convenience, we manufacture a solution $u(x, y) = \sin(\pi x)\sin(\pi y)$ and use the exact coefficient and solution to compute f . Assuming that measurements u^δ can be obtained from 100 sensors inside the domain and $\tilde{N}_{bd} = 25$ equally distributed sensors at each boundary for the Dirichlet boundary condition (see Figure 5(b)). To solve the problem, we use two independent DNNs with the same structure to parameterize a and u , respectively. We set $N_p = 200$, $topK = 150$, $K_{int} = 60$, and use Tanh as the activation for the ParticleWNN method. For a fair comparison, we use 12,000 ($topK = 9000$) collocation points for the vanilla PINN and keep other settings consistent with the ParticleWNN. For the VPINN method, we choose $N_{test} = 50$ test functions, $N_{int} = 225$ integration points, and keep other settings consistent with ParticleWNN.

We consider two different noise levels $\delta \sim \mathcal{N}(0, 0.01^2)$, $\delta \sim \mathcal{N}(0, 0.1^2)$. The experiment results are recorded in Table 4, and plots of the Relative error, MAE, and loss with respect to time are shown in Figure 5. The predicted coefficients and solutions obtained by different methods are illustrated in Figure 6. From Table 4, we observe that the vanilla PINN and the VPINN are very sensitive to noise, while the ParticleWNN achieves good results at both noise levels. Moreover, ParticleWNN converges much faster among these methods and takes less than half of the computation time of the vanilla PINN. This is also evident in Figure 5. Figure 6 also indicates that, although VPINN can obtain the solution very well, it struggles to invert the coefficients effectively.

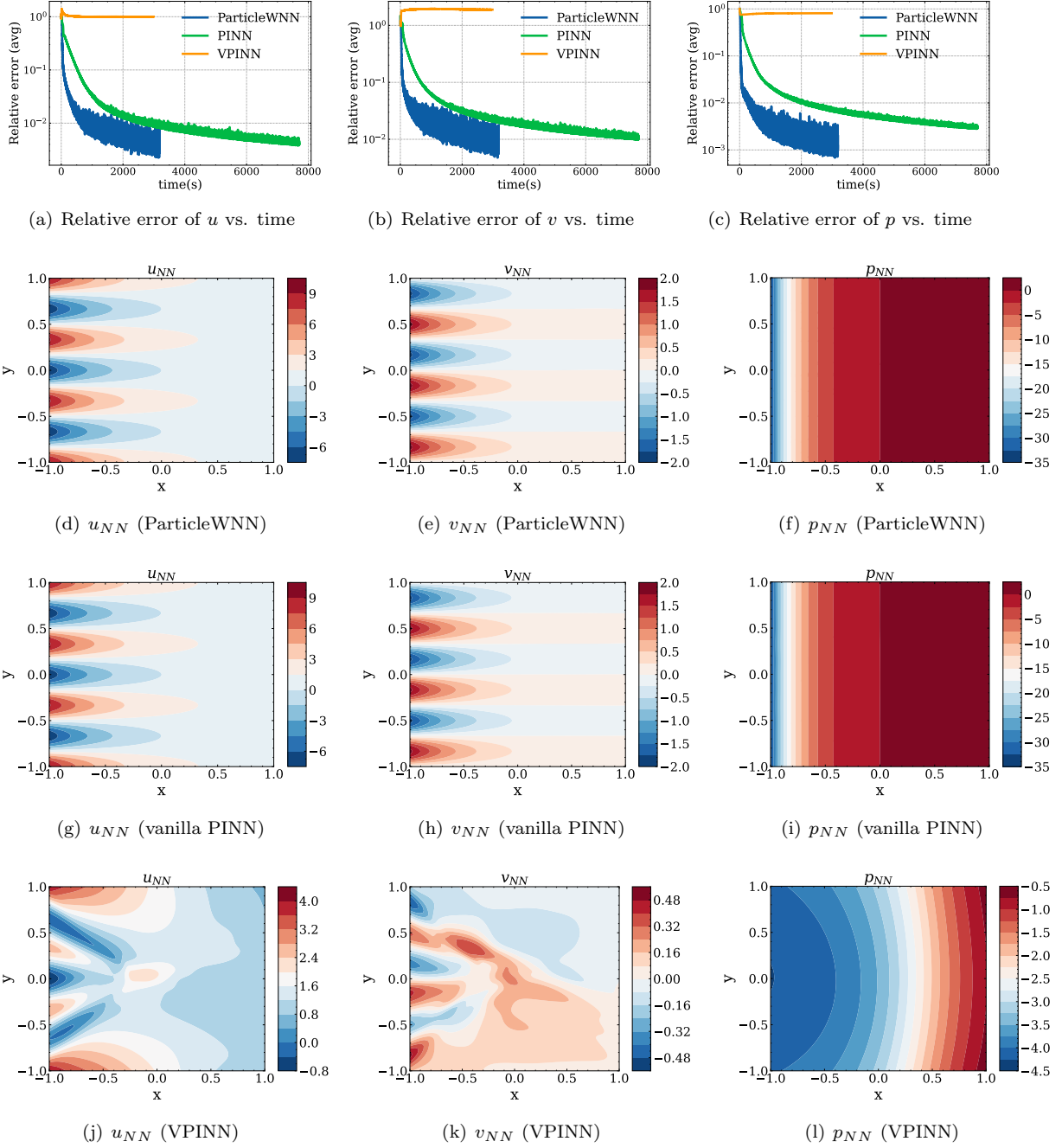


Figure 4: The performance of different methods in solving the steady NS problem (18). (a) The average Relative errors of u vs. the average times; (b) The average Relative errors of v vs. the average times; (c) The average Relative errors of p vs. the average times; (d), (e), (f) The average predicted u_{NN} , v_{NN} , and p_{NN} obtained by the ParticleWNN, respectively; (g), (h), (i) The average predicted u_{NN} , v_{NN} , and p_{NN} obtained by the vanilla PINN, respectively; (j), (k), (l) The average predicted u_{NN} , v_{NN} , and p_{NN} obtained by the VPINN, respectively.

Table 4: Experiment results for the inverse problem (20).

		ParticleWNN	vanilla PINN	VPINN
Noise level 0.01	Relative error for a	0.030 ± 0.003	0.663 ± 1.224	0.858 ± 0.475
	MAE for a	0.057 ± 0.006	0.384 ± 0.612	0.656 ± 0.145
	Relative error for u	0.009 ± 0.001	0.199 ± 0.367	0.022 ± 0.007
	MAE for u	0.018 ± 0.003	0.274 ± 0.477	0.082 ± 0.037
	Time (s)	232.82 ± 4.29	463.48 ± 2.09	308.96 ± 1.28
Noise level 0.1	Relative error for a	0.058 ± 0.006	0.337 ± 0.519	0.645 ± 0.080
	MAE for a	0.086 ± 0.008	0.309 ± 0.382	0.600 ± 0.059
	Relative error for u	0.024 ± 0.002	0.135 ± 0.218	0.031 ± 0.003
	MAE for u	0.049 ± 0.007	0.335 ± 0.569	0.093 ± 0.036
	Time (s)	228.15 ± 2.04	456.52 ± 0.54	305.46 ± 0.13

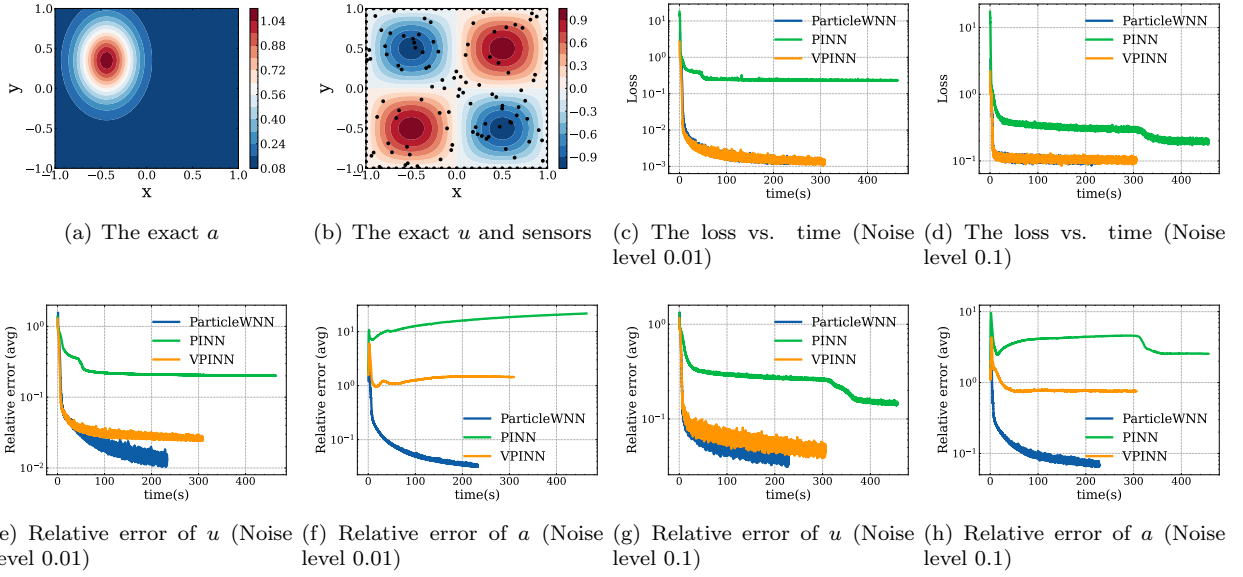


Figure 5: The performance of different methods in solving the inverse problem (20) with different noise levels. (a) The exact a ; (b) The exact u and sensors (black dots); (c), (d) The average Loss vs. the average computation time at noise level 0.01 and 0.1, respectively; (e), (f) The average Relative error vs. average computation time at noise level 0.01 for u and a , respectively; (g), (h) The average Relative error vs. average computation time at noise level 0.1 for u and a , respectively.

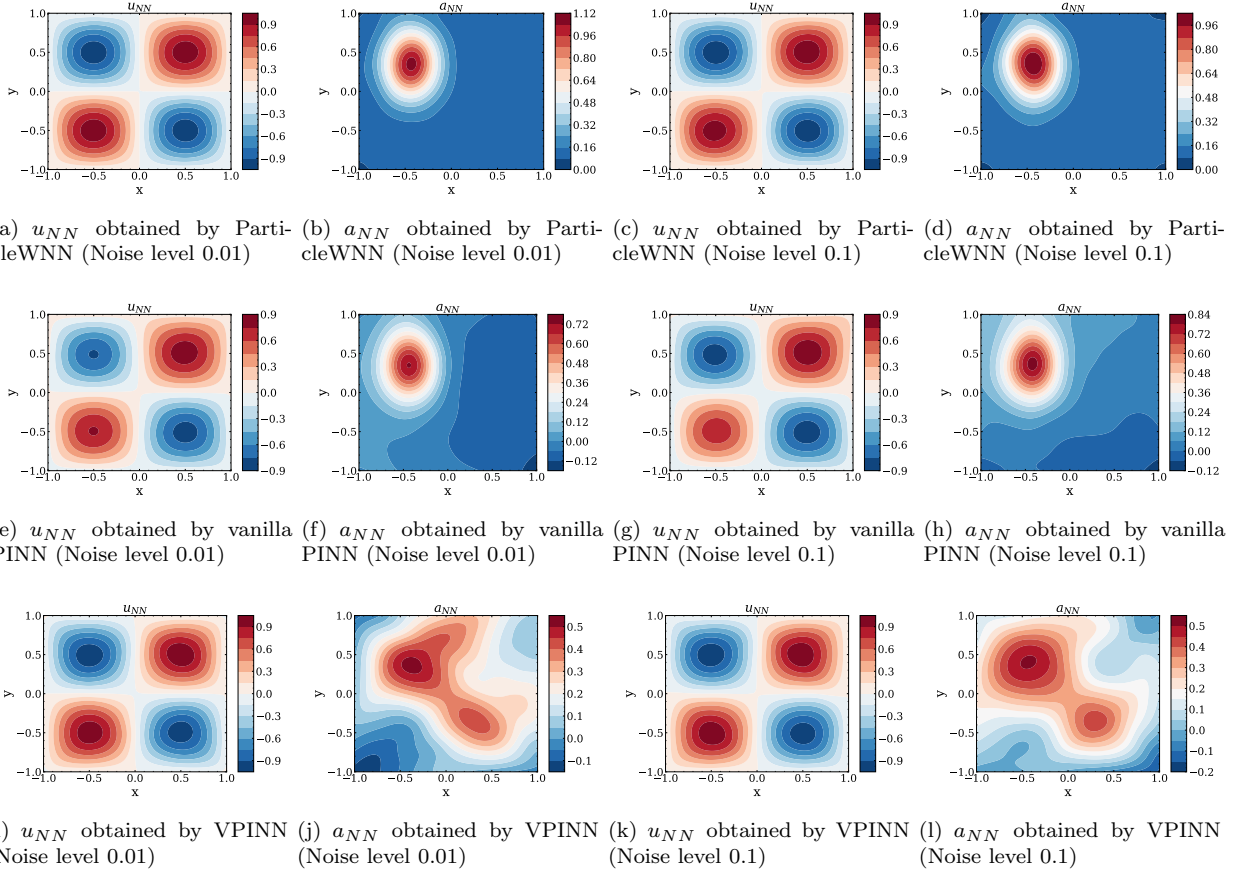


Figure 6: The performance of different methods in solving the inverse problem (20). (a), (b), (c), (d) The average u_{NN} , a_{NN} obtained by the ParticleWNN at noise level 0.01 and 0.1, respectively; (e), (f), (g), (h) The average u_{NN} , a_{NN} obtained by the vanilla PINN at noise level 0.01 and 0.1, respectively; (i), (j), (k), (l) The average u_{NN} , a_{NN} obtained by the VPINN at noise level 0.01 and 0.1, respectively.

5.5 A high-dimension example

Finally, we demonstrate ParticleWNN’s capability to handle high-dimensional problems by solving the following PDE with Dirichlet boundary conditions:

$$-\Delta u = f, \quad \mathbf{x} \in [-1, 1]^d \tag{22}$$

where $f = \sum_{i=1}^d x_i \sin(\pi x_{i+1})$ and $d = 5$. In the ParticleWNN method, we employ $N_p = 80$, $K_{int} = 1233$, and $\tilde{N}_{bd} = 100$. We use Tanh as the activation for the DNN model and keep other settings consistent with those in Section 5.1. For fairness, we generate $1233 * 80$ integration points for the DeepRitz method and $1233 * 80$ collocation points for the vanilla PINN method. Additionally, we use $N_{test} = 50$ test functions and $N_{int} = 1973$ integration points for the VPINN method, while keeping other parameters consistent with the ParticleWNN method.

After $maxIter = 20000$ iterations, the performance of each method is detailed in Table 5. From this table, we can see that the ParticleWNN method achieves both the smallest error and the shortest computation time. We also test ParticleWNN’s capacity to address higher-dimensional problems by considering the problem

Table 5: Experiment results for the high-dimension problem (22) with $d = 5$.

	ParticleWNN	vanilla PINN	VPINN	DeepRitz
Relative error	0.033 ± 0.002	0.036 ± 0.002	0.038 ± 0.001	0.431 ± 0.001
MAE	0.305 ± 0.031	0.270 ± 0.024	0.358 ± 0.043	1.364 ± 0.049
Time(s)	559.79 ± 1.61	3994.45 ± 2.64	589.31 ± 2.50	643.71 ± 15.74

(22) with $d = 10$. To adapt to this higher dimension, we reduce the number of neurons in each layer of the DNN to 25 while keeping the network’s overall structure unchanged. We then set $N_p = 80$, $N_{int} = 1161$, and $\tilde{N}_{bd} = 100$, with all other parameters remaining the same. After $maxIter = 50000$ iterations, the Relative error and MAE obtained by the ParticleWNN are 0.049 ± 0.001 and 0.783 ± 0.079 , respectively. This result demonstrates ParticleWNN’s robust performance in handling higher-dimensional problems.

5.6 Additional ablations

For weak-form DNN-based methods, the choice of the number of integration points and/or particles plays a pivotal role in algorithm performance. This decision involves finding the delicate balance between maximizing accuracy and minimizing computational effort when utilizing weak-form DNN-based methods for solving PDEs. Therefore, in this section, we delve into the impact of varying N_p and K_{int} on the ParticleWNN method. To conduct this investigation, we apply the ParticleWNN approach to solve the Poisson problem (15) with $\omega = 15\pi$. We set Since as the activation function and explore different combinations of N_p and K_{int} . Experimental results are presented in Figure 7, and detailed metrics such as relative errors, MAEs, and computation times can be found in Appendix C. From Figures 7(a) to 7(b), we observe that, within the context of our problem settings, achieving a satisfactory level of accuracy requires a minimum of 100 particles and a minimum of 10 integration points (summing up to 1000 points). This number of points is significantly lower than what other methods typically demand under similar conditions (as discussed in Section 5.1). However, it is important to note that the required number of particles and integration points may vary for different problems and parameter settings. For instance, problems with lower solution regularity may necessitate more points, and vice versa.

In summary, our ablation study indicates that increasing the number of points leads to higher accuracy, albeit with a linear increase in computation time (as illustrated in Figure 7(c)). Moreover, both the number of particles and integration points should not be set too small for effective performance.

6 Conclusion

In this work, we propose a novel framework, ParticleWNN, for solving PDEs in weak-form with DNNs. The novelty of the framework lies in the use of test functions compactly supported in extremely small regions.

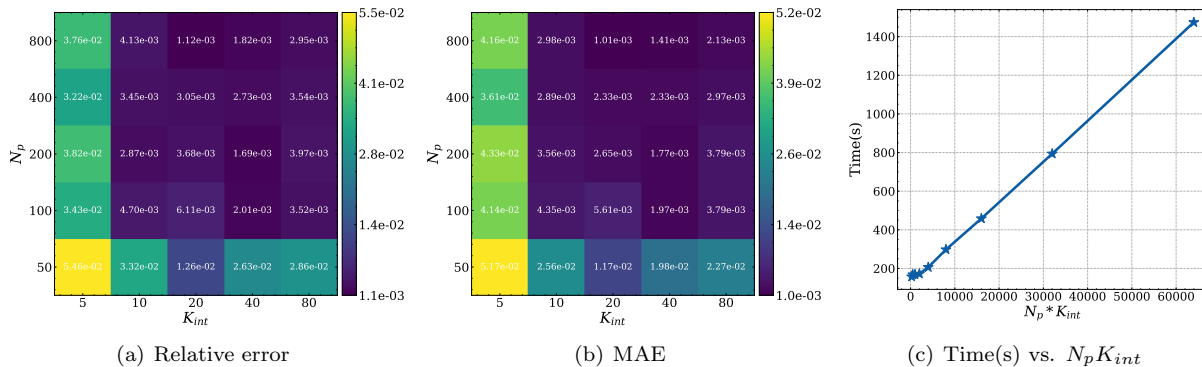


Figure 7: Performance of the ParticleWNN with different combinations of N_p and K_{int} . (a) Average Relative errors; (b) Average MAEs; (c) Average computation times vs. $N_p K_{int}$.

The sizes and locations of these support regions can be selected arbitrarily. In this way, the method not only inherits the advantages of weak-form methods such as requiring less regularity of the solution and a small number of quadrature points for computing the integrals, but also outperforms them in solving complicated solution problems. Additionally, the flexible definition of the test function makes ParticleWNN easily applicable for solving high-dimensional problems and complex domain problems. To improve the training of the ParticleWNN, several training strategies are developed, such as the R-descending strategy and adaptive selection of particles. Finally, we demonstrate the advantages of the ParticleWNN over other state-of-the-art methods in solving PDE problems and inverse problems.

While ParticleWNN avoids integrals over the entire domain or subdomains, it still encounters limitations imposed by integral calculations, such as errors caused by integral approximations. Therefore, an important future direction is to develop more efficient integral calculation techniques. Another future direction is to investigate new techniques to improve the ParticleWNN method, such as smarter particle selection rules [52, 53], more efficient training strategies [14, 54], and adaptive weighting strategies [55, 56].

Acknowledgement

We are grateful to Qian Huang for providing valuable feedbacks on the draft. The research of GB was supported in part by a National Natural Science of China grant (No. U21A20425) and a Key Laboratory of Zhejiang Province.

References

- [1] A. Vaswani, N. Shazeer, N. Parmar, J. Uszkoreit, L. Jones, A. N. Gomez, L. Kaiser, I. Polosukhin, Attention is all you need, *Advances in neural information processing systems* 30 (2017).
- [2] A. Voulodimos, N. Doulamis, A. Doulamis, E. Protopapadakis, et al., Deep learning for computer vision: A brief review, *Computational intelligence and neuroscience* 2018 (2018).
- [3] J. Jumper, R. Evans, A. Pritzel, T. Green, M. Figurnov, O. Ronneberger, K. Tunyasuvunakool, R. Bates, A. Žídek, A. Potapenko, et al., Highly accurate protein structure prediction with alphafold, *Nature* 596 (7873) (2021) 583–589.
- [4] J. Han, A. Jentzen, W. E, Solving high-dimensional partial differential equations using deep learning, *Proceedings of the National Academy of Sciences* 115 (34) (2018) 8505–8510.
- [5] J. Sirignano, K. Spiliopoulos, Dgm: A deep learning algorithm for solving partial differential equations, *Journal of computational physics* 375 (2018) 1339–1364.

- [6] Y. Zang, G. Bao, X. Ye, H. Zhou, Weak adversarial networks for high-dimensional partial differential equations, *Journal of Computational Physics* 411 (2020) 109409.
- [7] G. Bao, X. Ye, Y. Zang, H. Zhou, Numerical solution of inverse problems by weak adversarial networks, *Inverse Problems* 36 (11) (2020) 115003.
- [8] G.-J. Both, S. Choudhury, P. Sens, R. Kusters, Deepmod: Deep learning for model discovery in noisy data, *Journal of Computational Physics* 428 (2021) 109985.
- [9] H. Yan, J. Du, V. Y. Tan, J. Feng, On robustness of neural ordinary differential equations, arXiv preprint arXiv:1910.05513 (2019).
- [10] S. Mowlavi, S. Nabi, Optimal control of pdes using physics-informed neural networks, *Journal of Computational Physics* 473 (2023) 111731.
- [11] M. Raissi, P. Perdikaris, G. E. Karniadakis, Physics-informed neural networks: A deep learning framework for solving forward and inverse problems involving nonlinear partial differential equations, *Journal of Computational physics* 378 (2019) 686–707.
- [12] A. D. Jagtap, G. E. Karniadakis, Extended physics-informed neural networks (xpinns): A generalized space-time domain decomposition based deep learning framework for nonlinear partial differential equations., in: *AAAI Spring Symposium: MLPS, 2021*, pp. 2002–2041.
- [13] A. D. Jagtap, E. Kharazmi, G. E. Karniadakis, Conservative physics-informed neural networks on discrete domains for conservation laws: Applications to forward and inverse problems, *Computer Methods in Applied Mechanics and Engineering* 365 (2020) 113028.
- [14] A. Krishnapriyan, A. Gholami, S. Zhe, R. Kirby, M. W. Mahoney, Characterizing possible failure modes in physics-informed neural networks, *Advances in Neural Information Processing Systems* 34 (2021) 26548–26560.
- [15] B. Yu, et al., The deep ritz method: a deep learning-based numerical algorithm for solving variational problems, *Communications in Mathematics and Statistics* 6 (1) (2018) 1–12.
- [16] Y. Liao, P. Ming, Deep nitsche method: Deep ritz method with essential boundary conditions, arXiv preprint arXiv:1912.01309 (2019).
- [17] K. Li, K. Tang, T. Wu, Q. Liao, D3m: A deep domain decomposition method for partial differential equations, *IEEE Access* 8 (2019) 5283–5294.
- [18] R. Khodayi-Mehr, M. Zavlanos, Varnet: Variational neural networks for the solution of partial differential equations, in: *Learning for Dynamics and Control*, PMLR, 2020, pp. 298–307.
- [19] E. Kharazmi, Z. Zhang, G. E. Karniadakis, hp-vpinns: Variational physics-informed neural networks with domain decomposition, *Computer Methods in Applied Mechanics and Engineering* 374 (2021) 113547.
- [20] E. Kharazmi, Z. Zhang, G. E. Karniadakis, Variational physics-informed neural networks for solving partial differential equations, arXiv preprint arXiv:1912.00873 (2019).
- [21] G. Pang, L. Lu, G. E. Karniadakis, fpinns: Fractional physics-informed neural networks, *SIAM Journal on Scientific Computing* 41 (4) (2019) A2603–A2626.
- [22] X. Jin, S. Cai, H. Li, G. E. Karniadakis, Nsfnets (navier-stokes flow nets): Physics-informed neural networks for the incompressible navier-stokes equations, *Journal of Computational Physics* 426 (2021) 109951.
- [23] L. Yang, X. Meng, G. E. Karniadakis, B-pinns: Bayesian physics-informed neural networks for forward and inverse pde problems with noisy data, *Journal of Computational Physics* 425 (2021) 109913.

- [24] H. Gao, L. Sun, J.-X. Wang, Phygeonet: Physics-informed geometry-adaptive convolutional neural networks for solving parameterized steady-state pdes on irregular domain, *Journal of Computational Physics* 428 (2021) 110079.
- [25] C. Anitescu, E. Atroshchenko, N. Alajlan, T. Rabczuk, Artificial neural network methods for the solution of second order boundary value problems, *Computers, Materials and Continua* 59 (1) (2019) 345–359.
- [26] L. Lu, X. Meng, Z. Mao, G. E. Karniadakis, Deepxde: A deep learning library for solving differential equations, *SIAM review* 63 (1) (2021) 208–228.
- [27] R. G. Patel, I. Manickam, N. A. Trask, M. A. Wood, M. Lee, I. Tomas, E. C. Cyr, Thermodynamically consistent physics-informed neural networks for hyperbolic systems, *Journal of Computational Physics* 449 (2022) 110754.
- [28] J. Yu, L. Lu, X. Meng, G. E. Karniadakis, Gradient-enhanced physics-informed neural networks for forward and inverse pde problems, *Computer Methods in Applied Mechanics and Engineering* 393 (2022) 114823.
- [29] G. E. Karniadakis, I. G. Kevrekidis, L. Lu, P. Perdikaris, S. Wang, L. Yang, Physics-informed machine learning, *Nature Reviews Physics* 3 (6) (2021) 422–440.
- [30] J. Tompson, K. Schlachter, P. Sprechmann, K. Perlin, Accelerating eulerian fluid simulation with convolutional networks, in: *International Conference on Machine Learning*, PMLR, 2017, pp. 3424–3433.
- [31] R. Ranade, C. Hill, J. Pathak, Discretizationnet: A machine-learning based solver for navier–stokes equations using finite volume discretization, *Computer Methods in Applied Mechanics and Engineering* 378 (2021) 113722.
- [32] P.-H. Chiu, J. C. Wong, C. Ooi, M. H. Dao, Y.-S. Ong, Can-pinn: A fast physics-informed neural network based on coupled-automatic–numerical differentiation method, *Computer Methods in Applied Mechanics and Engineering* 395 (2022) 114909.
- [33] P. Ren, C. Rao, Y. Liu, J.-X. Wang, H. Sun, Phycrnet: Physics-informed convolutional-recurrent network for solving spatiotemporal pdes, *Computer Methods in Applied Mechanics and Engineering* 389 (2022) 114399.
- [34] N. Wandel, M. Weinmann, R. Klein, Learning incompressible fluid dynamics from scratch–towards fast, differentiable fluid models that generalize, *arXiv preprint arXiv:2006.08762* (2020).
- [35] H. Yao, Y. Gao, Y. Liu, Fea-net: A physics-guided data-driven model for efficient mechanical response prediction, *Computer Methods in Applied Mechanics and Engineering* 363 (2020) 112892.
- [36] Z. Li, N. Kovachki, K. Azizzadenesheli, B. Liu, K. Bhattacharya, A. Stuart, A. Anandkumar, Neural operator: Graph kernel network for partial differential equations, *arXiv preprint arXiv:2003.03485* (2020).
- [37] L. Lu, P. Jin, G. Pang, Z. Zhang, G. E. Karniadakis, Learning nonlinear operators via deepnet based on the universal approximation theorem of operators, *Nature machine intelligence* 3 (3) (2021) 218–229.
- [38] Z. Li, N. Kovachki, K. Azizzadenesheli, B. Liu, K. Bhattacharya, A. Stuart, A. Anandkumar, Fourier neural operator for parametric partial differential equations, *arXiv preprint arXiv:2010.08895* (2020).
- [39] Z. Li, N. Kovachki, K. Azizzadenesheli, B. Liu, A. Stuart, K. Bhattacharya, A. Anandkumar, Multipole graph neural operator for parametric partial differential equations, *Advances in Neural Information Processing Systems* 33 (2020) 6755–6766.
- [40] S. Cai, Z. Wang, L. Lu, T. A. Zaki, G. E. Karniadakis, Deepm&mnet: Inferring the electroconvection multiphysics fields based on operator approximation by neural networks, *Journal of Computational Physics* 436 (2021) 110296.

- [41] L. C. Evans, *Partial differential equations*, Vol. 19, American Mathematical Society, 2022.
- [42] E. Novak, K. Ritter, High dimensional integration of smooth functions over cubes, *Numerische Mathematik* 75 (1) (1996) 79–97.
- [43] W. J. Morokoff, R. E. Caflisch, Quasi-monte carlo integration, *Journal of computational physics* 122 (2) (1995) 218–230.
- [44] R. Fry, S. McManus, Smooth bump functions and the geometry of banach spaces: a brief survey, *Expositiones Mathematicae* 20 (2) (2002) 143–183.
- [45] H. Wendland, Piecewise polynomial, positive definite and compactly supported radial functions of minimal degree, *Advances in computational Mathematics* 4 (1995) 389–396.
- [46] Z. Wu, Compactly supported positive definite radial functions, *Advances in computational mathematics* 4 (1995) 283–292.
- [47] M. Buhmann, A new class of radial basis functions with compact support, *Mathematics of Computation* 70 (233) (2001) 307–318.
- [48] E. Bisong, E. Bisong, Google colaboratory, *Building machine learning and deep learning models on google cloud platform: a comprehensive guide for beginners* (2019) 59–64.
- [49] K. Banachewicz, L. Massaron, A. Goldbloom, *The Kaggle Book: Data analysis and machine learning for competitive data science*, Packt Publishing Ltd, 2022.
- [50] S. Basir, I. Senocak, Critical investigation of failure modes in physics-informed neural networks, in: *AIAA SCITECH 2022 Forum*, 2022, p. 2353.
- [51] P. G. Drazin, N. Riley, *The Navier-Stokes equations: a classification of flows and exact solutions*, no. 334, Cambridge University Press, 2006.
- [52] K. Tang, X. Wan, C. Yang, Das-pinns: A deep adaptive sampling method for solving high-dimensional partial differential equations, *Journal of Computational Physics* 476 (2023) 111868.
- [53] Z. Gao, L. Yan, T. Zhou, Failure-informed adaptive sampling for pinns, *SIAM Journal on Scientific Computing* 45 (4) (2023) A1971–A1994.
- [54] S. Wang, S. Sankaran, P. Perdikaris, Respecting causality is all you need for training physics-informed neural networks, *arXiv preprint arXiv:2203.07404* (2022).
- [55] S. Wang, Y. Teng, P. Perdikaris, Understanding and mitigating gradient pathologies in physics-informed neural networks, *arXiv preprint arXiv:2001.04536* (2020).
- [56] R. van der Meer, C. W. Oosterlee, A. Borovykh, Optimally weighted loss functions for solving pdes with neural networks, *Journal of Computational and Applied Mathematics* 405 (2022) 113887.

A The effect of the R-adaptive training strategy on the algorithm

To determine the most effective R-adaptive training strategy, we solve the Poisson problem with frequency $\omega = 15\pi$ in Section 5.1 using ParticleWNN with different R-adaptive strategies. For each strategy, we fix $R_{min} = 10^{-6}$, and then investigate the impact of varying R_{max} on the algorithm. The activation function is selected as *Since* and the remaining experimental settings are consistent with those in Section 5.1. We record the Relative errors and MAEs obtained by the ParticleWNN in Table 6 and Table 7, respectively. To gain a more intuitive understanding of the impact of the R-adaptive strategy and R_{max} on ParticleWNN, we visualize the Relative errors and the MAEs in Figure 8(a) and Figure 8(b), respectively. From 8(a) and 8(b), we can see that the ParticleWNN performs best with the R-descending strategy. Particularly, when the R-descending strategy is applied, ParticleWNN achieves the smallest average Relative error and MAE at $R_{max} = 10^{-4}$.

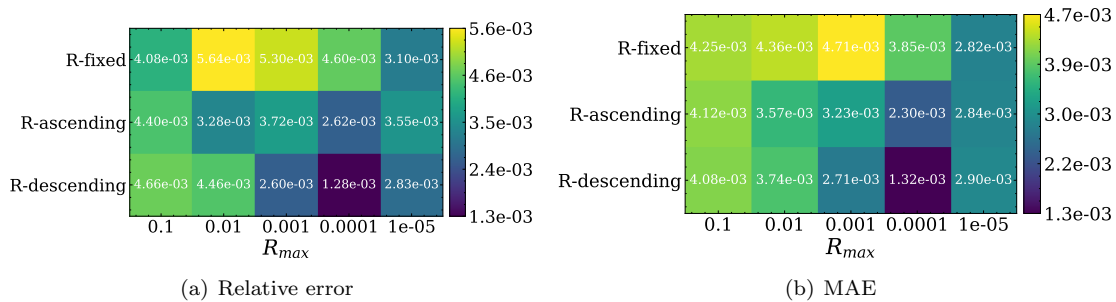


Figure 8: The performance of the ParticleWNN under different R-adaptive strategies and R_{max} . (a) Average Relative errors; (b) Average MAEs.

Table 6: Relative errors obtained by the ParticleWNN under different combinations of R-adaptive strategy and R_{max} .

	R_{max}				
	$1e^{-1}$	$1e^{-2}$	$1e^{-3}$	$1e^{-4}$	$1e^{-5}$
R-fixed	$4.1e^{-3} \pm 1.5e^{-3}$	$5.6e^{-3} \pm 5.6e^{-3}$	$5.3e^{-3} \pm 3.1e^{-3}$	$4.6e^{-3} \pm 4.6e^{-3}$	$3.1e^{-3} \pm 1.2e^{-3}$
R-ascending	$4.4e^{-3} \pm 3.0e^{-3}$	$3.3e^{-3} \pm 1.6e^{-3}$	$3.7e^{-3} \pm 3.0e^{-3}$	$2.6e^{-3} \pm 2.6e^{-3}$	$3.5e^{-3} \pm 2.0e^{-3}$
R-descending	$4.6e^{-3} \pm 1.8e^{-3}$	$4.5e^{-3} \pm 4.2e^{-3}$	$2.6e^{-3} \pm 1.6e^{-3}$	$1.3e^{-3} \pm 1.1e^{-3}$	$2.8e^{-3} \pm 2.3e^{-3}$

Table 7: MAEs obtained by the ParticleWNN under different combinations of R-adaptive strategy and R_{max} .

	R_{max}				
	$1e^{-1}$	$1e^{-2}$	$1e^{-3}$	$1e^{-4}$	$1e^{-5}$
R-fixed	$4.3e^{-3} \pm 1.3e^{-3}$	$4.4e^{-3} \pm 3.1e^{-3}$	$4.7e^{-3} \pm 2.2e^{-3}$	$3.8e^{-3} \pm 3.7e^{-3}$	$2.8e^{-3} \pm 1.1e^{-3}$
R-ascending	$4.1e^{-3} \pm 2.0e^{-3}$	$3.6e^{-3} \pm 2.3e^{-3}$	$3.2e^{-3} \pm 2.4e^{-3}$	$2.3e^{-3} \pm 2.0e^{-3}$	$2.8e^{-3} \pm 1.2e^{-3}$
R-descending	$4.1e^{-3} \pm 1.7e^{-3}$	$3.7e^{-3} \pm 2.8e^{-3}$	$2.7e^{-3} \pm 1.7e^{-3}$	$1.3e^{-3} \pm 9.8e^{-4}$	$2.9e^{-3} \pm 2.4e^{-3}$

B The effect of the adaptive particle selection technique on the algorithm

In this section, we examine the effect of the *topK* adaptive particle selection technique on the ParticleWNN approach. We set $topK = 200$ and vary N_p between 200, 250, 300, 350 and 400, and then employ ParticleWNN to solve the Poisson problem (15) with frequency $\omega = 15\pi$ in Section 5.1. We select the activation as *Since* and keep other parameters consistent with those used in Section 5.1. The experimental results are illustrated in Figure 9, and the Relative errors and MAEs are recorded in Table 8. From Figure 9, we can see that a

suitable selection of N_p (e.g., $N_p = 300$) with $topK = 200$ has a positive effect on the algorithm’s convergence and accuracy. When $N_p \leq 300$ ($topK = 200$), Figure 9(c) shows that the $topK$ technique obviously improves the convergence and accuracy of the algorithm.

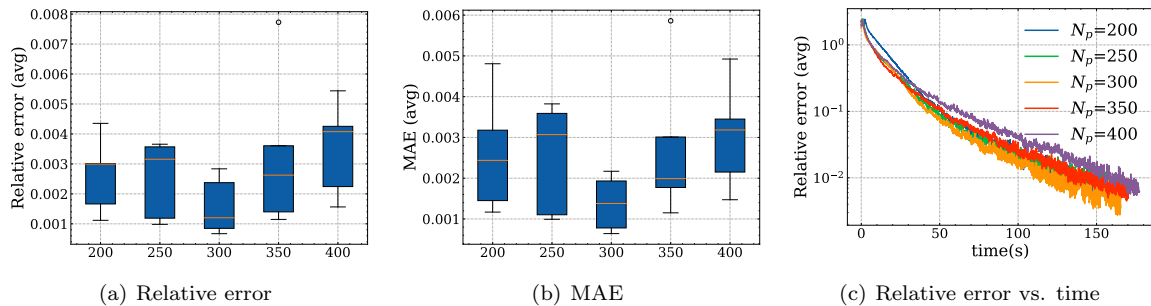


Figure 9: Performance of the ParticleWNN under different N_p ($topK = 200$). (a) Average Relative errors; (b) Average MAEs. (c) Average Relative error vs. Average computation times.

Table 8: Relative errors and MAEs obtained by the ParticleWNN under different N_p ($topK = 200$).

	$N_p = 200$	$N_p = 250$	$N_p = 300$	$N_p = 350$	$N_p = 400$
Relative error	$2.6e^{-3} \pm 1.1e^{-3}$	$2.5e^{-3} \pm 1.2e^{-3}$	$1.6e^{-3} \pm 8.6e^{-4}$	$3.3e^{-3} \pm 2.4e^{-3}$	$3.5e^{-3} \pm 1.4e^{-3}$
MAE	$2.6e^{-3} \pm 1.3e^{-3}$	$2.5e^{-3} \pm 1.2e^{-3}$	$1.4e^{-3} \pm 6.1e^{-4}$	$2.7e^{-3} \pm 1.7e^{-3}$	$3.0e^{-3} \pm 1.2e^{-3}$

C Additional ablations

The Relative errors, MAEs, and time consumptions obtained by the ParticleWNN in Section 5.6 are recorded in Table 9, Table 10, and Table 11, respectively. Additionally, the visual representations of the Relative errors, MAEs, and computation times are provided in Figures 10(a), 10(b), and 10(c), respectively.

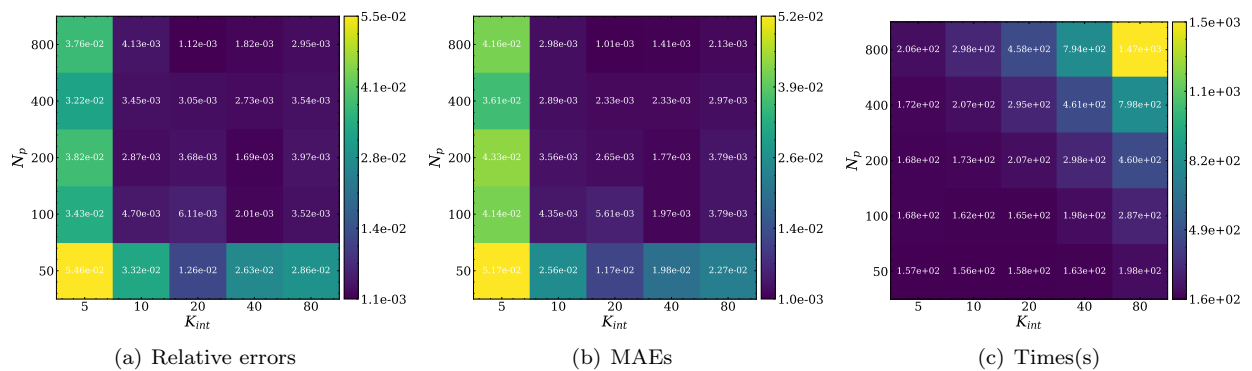


Figure 10: Performance of the ParticleWNN with different combinations of N_p and K_{int} . (a) Average Relative errors; (b) Average MAEs; (c) Average computation times.

Table 9: Relative errors obtained by the ParticleWNN under different combinations of N_p and K_{int} .

$N_p \backslash K_{int}$	5	10	20	40	80
800	$3.7e^{-2} \pm 3.4e^{-3}$	$4.1e^{-3} \pm 4.5e^{-3}$	$1.1e^{-3} \pm 0.3e^{-3}$	$1.8e^{-3} \pm 1.0e^{-3}$	$2.9e^{-3} \pm 1.1e^{-3}$
400	$3.2e^{-2} \pm 5.2e^{-3}$	$3.5e^{-3} \pm 2.8e^{-3}$	$3.0e^{-3} \pm 3.4e^{-3}$	$2.7e^{-3} \pm 1.9e^{-3}$	$3.5e^{-3} \pm 4.2e^{-3}$
200	$3.8e^{-2} \pm 3.8e^{-3}$	$2.9e^{-3} \pm 1.3e^{-3}$	$3.7e^{-3} \pm 2.1e^{-3}$	$1.7e^{-3} \pm 0.5e^{-4}$	$3.9e^{-3} \pm 2.4e^{-3}$
100	$3.4e^{-2} \pm 3.2e^{-3}$	$4.7e^{-3} \pm 3.7e^{-3}$	$6.1e^{-3} \pm 3.2e^{-3}$	$2.0e^{-3} \pm 0.4e^{-4}$	$3.5e^{-3} \pm 1.9e^{-3}$
50	$5.4e^{-2} \pm 1.4e^{-2}$	$3.3e^{-2} \pm 2.1e^{-2}$	$1.3e^{-2} \pm 5.6e^{-3}$	$2.6e^{-2} \pm 1.8e^{-2}$	$2.8e^{-2} \pm 2.4e^{-2}$

Table 10: MAEs obtained by the ParticleWNN under different combinations of N_p and K_{int} .

$N_p \backslash K_{int}$	5	10	20	40	80
800	$4.2e^{-2} \pm 2.7e^{-3}$	$2.9e^{-3} \pm 2.3e^{-3}$	$1.0e^{-3} \pm 4.7e^{-4}$	$1.4e^{-3} \pm 5.3e^{-4}$	$2.1e^{-3} \pm 7.3e^{-4}$
400	$3.6e^{-2} \pm 6.7e^{-3}$	$2.8e^{-3} \pm 1.6e^{-3}$	$2.3e^{-3} \pm 2.1e^{-3}$	$2.3e^{-3} \pm 1.2e^{-3}$	$2.9e^{-3} \pm 2.6e^{-3}$
200	$4.3e^{-2} \pm 2.3e^{-3}$	$3.5e^{-3} \pm 2.1e^{-3}$	$2.6e^{-3} \pm 1.3e^{-3}$	$1.7e^{-3} \pm 5.4e^{-4}$	$3.8e^{-3} \pm 2.0e^{-3}$
100	$4.1e^{-2} \pm 3.1e^{-3}$	$4.3e^{-3} \pm 2.9e^{-3}$	$5.6e^{-3} \pm 2.6e^{-3}$	$1.9e^{-3} \pm 4.1e^{-4}$	$3.8e^{-3} \pm 2.2e^{-3}$
50	$5.2e^{-2} \pm 5.3e^{-3}$	$2.5e^{-2} \pm 1.5e^{-2}$	$1.2e^{-2} \pm 4.2e^{-3}$	$1.9e^{-2} \pm 1.6e^{-2}$	$2.3e^{-2} \pm 1.5e^{-2}$

Table 11: Time consumptions of the ParticleWNN under different combinations of N_p and K_{int} .

$N_p \backslash K_{int}$	5	10	20	40	80
800	206.2 ± 5.7	297.7 ± 3.2	458.3 ± 2.6	793.8 ± 11.0	1474.2 ± 12.2
400	172.1 ± 12.6	206.5 ± 13.1	294.6 ± 7.9	461.0 ± 11.7	789.3 ± 9.8
200	168.3 ± 10.6	173.0 ± 12.5	207.0 ± 9.2	297.8 ± 9.7	460.2 ± 7.5
100	167.9 ± 8.5	161.9 ± 4.9	165.4 ± 3.5	198.2 ± 3.2	287.2 ± 2.0
50	157.4 ± 4.7	156.0 ± 3.2	157.6 ± 3.9	162.6 ± 3.5	197.6 ± 2.9